Article

Uniquantal Release through a Dynamic Fusion Pore Is a Candidate Mechanism of Hair Cell Exocytosis

Nikolai M. Chapochnikov,[1,2,3,9] Hideki Takago,[1,4,9] Chao-Hua Huang,[1,5] Tina Pangršič,[1,5] Darina Khimich,[1] Jakob Neef,[1,5] Elisabeth Auge,[1,6] Fabian Göttfert,[7] Stefan W. Hell,[7,8] Carolin Wichmann,[1,5,6,*] Fred Wolf,[2,3,5,*] and Tobias Moser[1,2,5,8,*]

[1]InnerEarLab, Department of Otolaryngology, University Medical Center Göttingen, 37075 Göttingen, Germany
[2]Bernstein Center for Computational Neuroscience, University of Göttingen, 37073 Göttingen, Germany
[3]Max Planck Institute for Dynamics and Self-Organization, 37077 Göttingen, Germany
[4]Department of Rehabilitation for Sensory Functions, Research Institute, National Rehabilitation Center for Persons with Disabilities, Saitama 359-8555, Japan
[5]Collaborative Research Center 889 Cellular Mechanisms of Sensory Processing, 37099 Göttingen, Germany
[6]Molecular Architecture of Synapses Junior Research Group, University Medical Center Göttingen, 37075 Göttingen, Germany
[7]Department of Nanobiophotonics, Max Planck Institute for Biophysical Chemistry, 37077 Göttingen, Germany
[8]Center for Nanoscale Microscopy and Molecular Physiology of the Brain, University of Göttingen, 37073 Göttingen, Germany
[9]Co-first author
*Correspondence: cwichma@gwdg.de (C.W.), fred@nld.ds.mpg.de (F.W.), tmoser@gwdg.de (T.M.)
http://dx.doi.org/10.1016/j.neuron.2014.08.003

SUMMARY

The mechanisms underlying the large amplitudes and heterogeneity of excitatory postsynaptic currents (EPSCs) at inner hair cell (IHC) ribbon synapses are unknown. Based on electrophysiology, electron and superresolution light microscopy, and modeling, we propose that uniquantal exocytosis shaped by a dynamic fusion pore is a candidate neurotransmitter release mechanism in IHCs. Modeling indicated that the extended postsynaptic AMPA receptor clusters enable large uniquantal EPSCs. Recorded multiphasic EPSCs were triggered by similar glutamate amounts as monophasic ones and were consistent with progressive vesicle emptying during pore flickering. The fraction of multiphasic EPSCs decreased in absence of Ca^{2+} influx and upon application of the Ca^{2+} channel modulator BayK8644. Our experiments and modeling did not support the two most popular multiquantal release interpretations of EPSC heterogeneity: (1) Ca^{2+}-synchronized exocytosis of multiple vesicles and (2) compound exocytosis fueled by vesicle-to-vesicle fusion. We propose that IHC synapses efficiently use uniquantal glutamate release for achieving high information transmission rates.

INTRODUCTION

In the classical framework of synaptic transmission, Ca^{2+} influx triggers the independent fusion of single synaptic vesicles (SVs) with the cell membrane (Katz and Miledi, 1965; uniquantal release, UQR). In this framework, the release of each SV is an all-or-none event for which only the probability is controlled. In recent years, however, several studies indicated that synapses also use strategies to modulate individual release events (Liu, 2003). For example, homotypic SV fusion was reported to increase quantal size during strong stimulation (e.g., He et al., 2009; multiquantal release, MQR). Moreover, the amount and kinetics of release can be controlled via the SV's fusion pore (Grabner and Zenisek, 2013; Pawlu et al., 2004; Rahamimoff and Fernandez, 1997; Staal et al., 2004).

Ribbon synapses (Figure 1A), which tonically release transmitter at a rate dependent on the graded presynaptic potential, also seem to modulate the amplitude and kinetics of individual release events, as reflected in the heterogeneity of their excitatory postsynaptic currents (EPSCs). This heterogeneity has been suggested to arise from synchronous MQR (Andor-Ardó et al., 2010; Glowatzki and Fuchs, 2002; Goutman and Glowatzki, 2007; Grant et al., 2010; Graydon et al., 2011; Keen and Hudspeth, 2006; Li et al., 2009; Matthews and Sterling, 2008; Mehta et al., 2013; Neef et al., 2007; Schnee et al., 2013; Siegel, 1992; Singer et al., 2004; Suryanarayanan and Slaughter, 2006). MQR at ribbon synapses was initially postulated for inner hair cells (IHCs) primarily because of the presence of very large monophasic EPSCs (up to 800 pA, mean: 300 pA) and multiphasic EPSC waveforms, which were interpreted to reflect highly and poorly synchronized SV release, respectively (Glowatzki and Fuchs, 2002). Contrary to MQR in spiking neurons (Wadiche and Jahr, 2001), MQR at ribbon synapses would occur without the synchronizing action of a presynaptic action potential.

Deciphering the mechanism of exocytosis at this first synapse in the auditory system is essential to understand how sound is encoded. Two main candidate mechanisms of MQR have been proposed for ribbon synapses: (1) release site-coordination (Glowatzki and Fuchs, 2002; Singer et al., 2004), which could be realized by synchronized triggering of multiple SVs by a common "Ca^{2+} nanodomain" around a single channel (Graydon et al., 2011; Jarsky et al., 2010; Figure 1B); (2) exocytosis of compound SVs generated by prior SV-to-SV (homotypic) fusion (Edmonds et al., 2004; He et al., 2009; Matthews and Sterling, 2008; Pickett and Edwardson, 2006; Figure 1C). However, so far no study
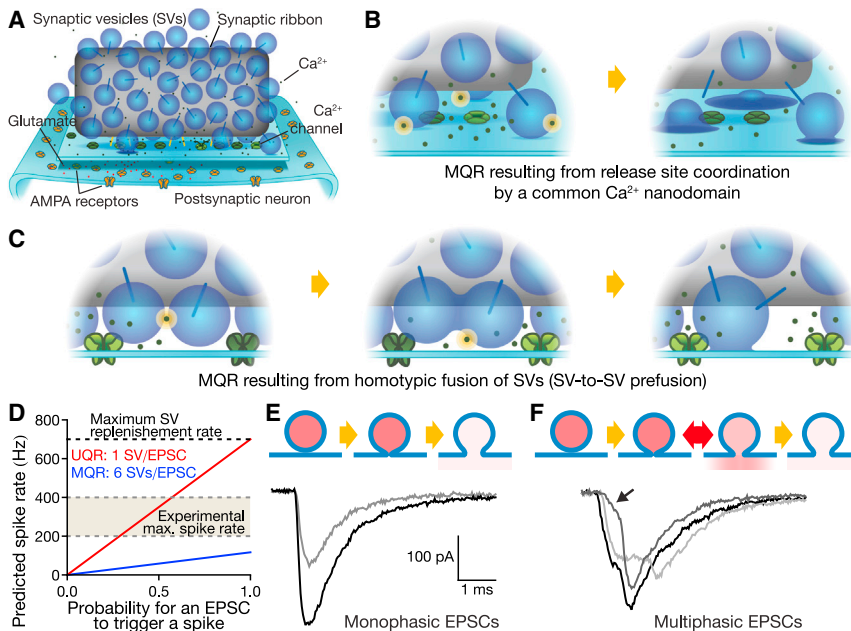
Figure 1. MQR and UQR Hypotheses at the IHC Ribbon Synapse

(A) Schematic of an IHC synapse. The ribbon (gray) tethers (blue sticks) SVs (blue spheres). Ca^{2+} ions (green dots) enter through Ca^{2+} channels (green pores) and trigger the exocytosis of docked SVs via activation of the Ca^{2+} sensor(s) of fusion. Open Ca^{2+} channels are depicted in light green, closed ones in dark green. Fusing SVs release their glutamate content (red dots) into the synaptic cleft. Glutamate binding to AMPARs (orange pores) on the SGN elicits their opening and EPSC generation. Ca^{2+} ions and channels are not drawn to scale.

(B) Scheme of the "Ca^{2+}-synchronized MQR" scenario. Left: Ca^{2+} channel opening elicits the entry of Ca^{2+} ions. Ca^{2+} binding to the Ca^{2+} sensors (yellow) triggers the release of three nearby docked SVs. Right: SVs exocytose at slightly different times. Such a multiquantal release would trigger an EPSC about three times the amplitude of a uniquantal EPSC.

(C) Scheme of the homotypic fusion scenario of MQR. The homotypic fusion of two SVs (left) creates a larger compound (middle), which then fuses with the plasma membrane (right). This event would generate an EPSC about twice the amplitude of a uniquantal EPSC.

(D) Predicted steady-state spike rate in MQR (blue) and UQR (red) scenarios as a function of the probability for an EPSC to trigger a spike. The SV replenishment rate was 700 Hz. The experimental steady-state spike rate was set to 200–400 Hz.

(E) UQR scenario: monophasic EPSCs result from the exocytosis of single SVs, with the whole glutamate content released at once.

(F) UQR scenario: multiphasic EPSCs result from the exocytosis of single SVs, occurring with subsequent fusion pore openings and closings, and/or variations in pore diameter. Some multiphasic EPSCs were reminiscent of "foot events" (black arrow).

could conclusively identify the mechanism underlying EPSC heterogeneity at IHC ribbon synapses. Here, combining electrophysiology, immunochemistry, electron and stimulated emission depletion (STED) microscopy, EPSC deconvolution, and biophysical modeling we show that a fundamentally different mechanism based on UQR and fusion pore dynamics can explain experimental observations at the IHC synapse, for which neither Ca^{2+}-synchronization nor compound exocytosis can account. We argue that UQR combined with a highly sensitive postsynaptic detector enables energetically efficient transmission at IHC ribbon synapses.

RESULTS

Uniquantal Release at the IHC Ribbon Synapse?

MQR is the current paradigm of IHC synapse operation. However, MQR appears improbable when comparing sound-driven spike rates in spiral ganglion neurons (SGNs) with presynaptic release rates of IHC active zones (AZs; Figure 1D). The maximal reported sustained SV release rate per AZ is approximately 700 Hz (Pangrsic et al., 2010) and on average six SVs compose an EPSC in the MQR scenario (Grant et al., 2010). Because one EPSC can trigger only one spike (Rutherford et al., 2012), a maximum spike rate of ~120 Hz is predicted. Yet, each IHC synapse can drive SGN spiking at 200–400 Hz during ongoing stimulation in vivo (Taberner and Liberman, 2005), where IHC depolarization likely is weaker. In an UQR scenario, on the other hand, these spiking rates would be easily achieved. Therefore,

we examined whether, alternatively, UQR might govern exocytosis at this synapse.

First, we performed an extensive analysis of EPSCs recorded from postsynaptic SGN boutons in rats (n = 4 for postnatal day 16 [P16] to P18, n = 1 for P10; Figures 1E, 1F, 2, and 4). We selected recordings with stable baseline and more than hundred EPSCs each (357 ± 168 EPSCs per SGN, n = 5). EPSCs from the IHC synapse have been classified into monophasic and multiphasic EPSCs according to their shape (Glowatzki and Fuchs, 2002; Figures 1E and 1F). We found many multiphasic EPSCs whose shape resembled "foot events" (black arrow, Figure 1F) recorded in adrenal chromaffin cells, where full release from a single large dense core vesicle is often preceded by a small pedestal or foot arising from a release through the nascent fusion pore (Albillos et al., 1997; Chow et al., 1992). We examined whether (1) large monophasic EPSCs could result from full and instantaneous release of single SVs (Figure 1E), and (2) multiphasic EPSCs could reflect release through a dynamic fusion pore (Figure 1F), which governs release also at other synapses (Grabner and Zenisek, 2013; Pawlu et al., 2004; Staal et al., 2004).

Different EPSC Waveforms Are Triggered by Similar Amounts of Glutamate

In the UQR hypothesis, each exocytosis event is triggered by a single SV, therefore, the different EPSC sizes and shapes are predicted to be elicited by, on average, a similar glutamate amount. To assess this, we first studied the EPSC amplitude
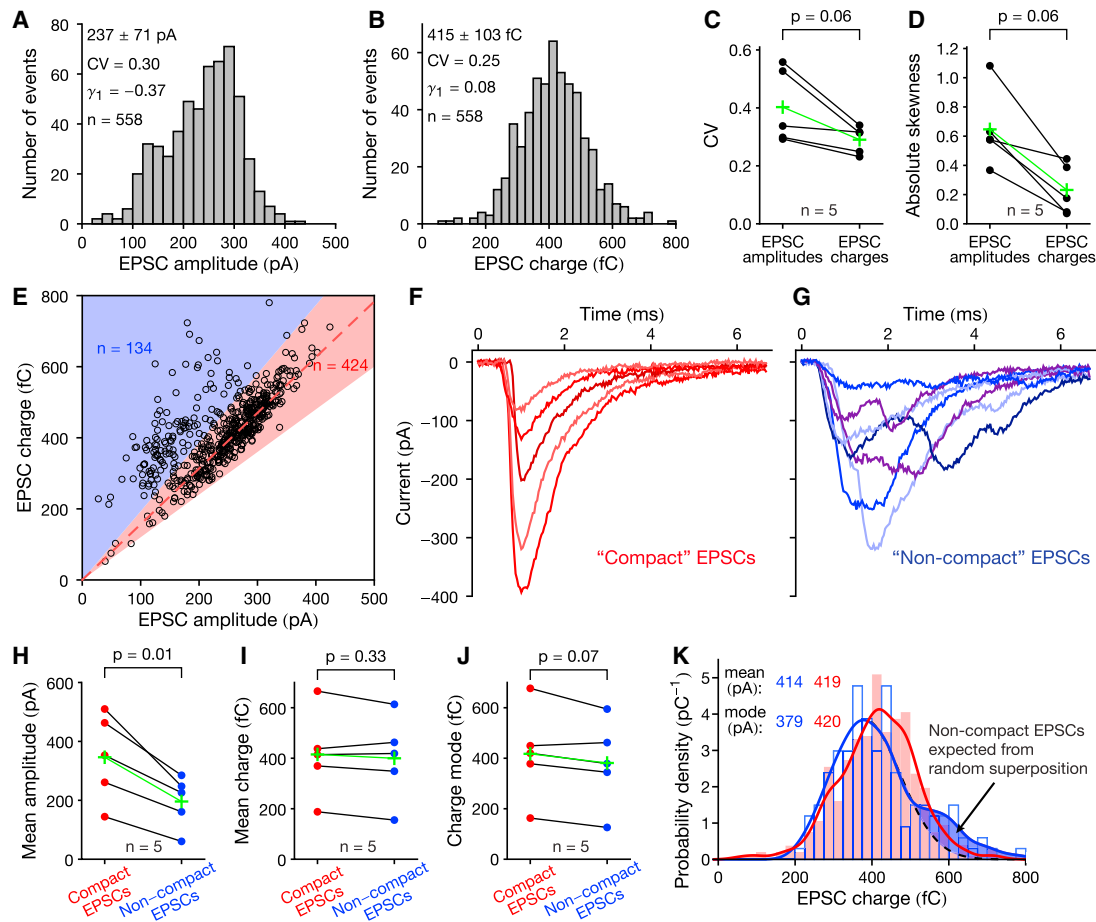
Figure 2. Compact and Non-compact EPSCs Are Triggered by Similar Glutamate Amounts

(A and B) Distribution of spontaneous EPSC amplitudes and charges from a single SGN. γ_1 stands for the skewness.

(C and D) CV (C) and absolute skewness (D) of EPSC amplitude versus charge distributions for five SGNs. The crosses indicate means.

(E) Scatter plot of EPSC charge versus EPSC amplitude from the same SGN as in (A) and (B). The red and blue background regions define compact and non-compact EPSCs, respectively. The red dashed line passes through the right point cloud. No EPSC appears in the white background region because the EPSC charge has a lower bound for a given amplitude.

(F and G) Examples of EPSCs taken from the red and blue regions of (E).

(H) Mean amplitude of compact versus non-compact EPSC for five SGNs.

(I) Mean charge of compact versus non-compact EPSC for five SGNs.

(J) Mode of the charge distributions of compact versus non-compact EPSC for five SGNs.

(K) Bar and smoothed histograms (plain lines) of compact (red) and non-compact (blue) EPSC charges. A normal distribution was superimposed on the right side of the non-compact EPSC charge distribution (dashed black). The blue area between the blue line and the dashed-black line corresponds to ~18 EPSCs. Calculating the number of non-compact EPSCs expected from random superposition we obtained ~13 EPSCs, close to 18.

Wilcoxon signed-rank test in (C) and (D) and paired t test in (H)–(J).

and charge distributions (Figures 2A–2D). The mean amplitude and charge among cells were 281 ± 123 pA and 404 ± 164 fC, respectively (n = 5). Charge distributions, which are a better proxy for glutamate content than amplitude distributions, were narrower (smaller coefficient of variation [CV]) and more symmetric (smaller absolute skewness) than amplitude distributions and displayed only one peak, compatible with a uniquantal charge distribution (del Castillo and Katz, 1954).

Plotting EPSC charge versus EPSC amplitude (Figure 2E; Figure S2 available online) revealed that in contrast to other synapses (e.g., Rossi et al., 1994), not all the points were aligned on

one diagonal (red dashed line). Instead, we found two elongated high-density regions in the scatter plot of each SGN. In the right region (red, Figures 2E and 2F), EPSCs have the largest amplitude for a given charge. They largely represented monophasic EPSCs, which we preferred to label "compact EPSCs" because they were briefer than other EPSCs. In the left region (blue, Figures 2E and 2G), EPSCs of similar charge were smaller and temporally more extended ("non-compact EPSCs"). They mainly represented multiphasic EPSCs, although some non-compact EPSCs had only one peak. Some points were interspersed between the two high-density regions, hampering an

automated separation between compact and non-compact EPSCs. We thus performed the separation by visual inspection with a line (border between the blue and red areas) passing through the origin (0 pA, 0 fC).

Next, we compared the amplitude and charge distributions of compact and non-compact EPSCs. The mean amplitude of compact EPSCs was significantly larger than that of non-compact ones in all SGNs (Figure 2H, p = 0.01) but the mean charge was comparable (Figure 2I, p = 0.33). We then compared the modes of the charge distributions because this measure is not influenced by the exact separation between compact and non-compact EPSCs or by outliers (Figure 2J). In fact, some "outlier" non-compact EPSCs are expected to result from random superposition of independent EPSCs. Such EPSCs influence the mean, but not the mode (Figure 2K). The mode of the charge distributions of non-compact EPSCs was on average 10% smaller (p = 0.07). In fact, a temporally spread release is expected to elicit an EPSC with a smaller charge than an instantaneous release because of the sublinear relation between EPSC amplitude and glutamate amount released for concentrations that are far from saturating the AMPA receptors (AMPARs, Figures 3E, 3F, and 3I). We conclude that compact and non-compact EPSCs are triggered by similar transmitter amounts, as expected for UQR.

Big AMPAR Clusters Enable Large Uniquantal EPSCs, and a Dynamic Fusion Pore Can Account for Complex EPSC Waveforms

A crucial test for the UQR hypothesis is whether the release of the glutamate content of a single SV can trigger large EPSCs. We approached this question by experimentally constrained biophysical simulations of glutamate release. A major determinant of the EPSC amplitude is the size of the postsynaptic receptor cluster (Nusser et al., 1997). Therefore, we studied the size and shape of SGN AMPAR clusters and their position relative to the IHC AZ using two-color STED microscopy of immunolabeled IHC synapses. Synapses imaged en-face exhibited the previously reported ring-like AMPAR clusters (Meyer et al., 2009; Figure 3A, first two columns) and in all images the AMPAR cluster tightly embraced the opposing AZ (Figure 3A), probably beneficial for the efficient detection of released glutamate. The annulus peak-to-peak distance in en-face imaged AMPAR clusters was 902 ± 126 nm (Figure 3B). We constructed the average cross-section of the AMPAR density (Figure 3C, green) using line profiles from en-face images (Figure 3A, white dashed lines) adjusted in length for alignment at their side peaks (white crosses). The immunofluorescence in the center was ~40% of the peak.

Next, we simulated EPSCs using a molecular model of glutamate release into the synaptic cleft, glutamate diffusion, and AMPAR binding and gating (Figure 3D; Table S1). The model approximated the postsynaptic AMPAR distribution (Figure 3C, orange; Figure S1A) by matching the average AMPAR density to published estimates (Saito, 1990). We computed the EPSC amplitude as a function of the SV glutamate content and postsynaptic AMPAR cluster size, with release in the center of the AMPAR cluster. We used the AMPAR kinetic schemes established from cerebellar synapses (Häusser and Roth, 1997) and

from rat calyx of Held auditory synapses (Budisantoso et al., 2013; Figures 3E and 3F). Estimates of SV content vary between ~1,000 and ~4,300 glutamates (Orrego and Villanueva, 1993; Riveros et al., 1986; Savtchenko et al., 2013; Takamori et al., 2006). We simulated the range from 500 to 7,000 glutamates, as the latter amount was found necessary to reproduce mEPSC amplitudes in the calyx of Held (AMPAR scheme of Figure 3F; Budisantoso et al., 2013). The UQR scenario would be plausible if a single SV can trigger large EPSC amplitudes (mean monophasic EPSC size: 295 ± 130 pA; Grant et al., 2010). For an average AMPAR cluster of ~900 nm peak-to-peak length, the release model reproduced EPSC sizes of 200–400 pA with glutamate amounts within the range of published values (2,300–3,800 and 4,000–6,800 for the two AMPAR schemes, respectively).

Next, we studied how the EPSC amplitude depends on the position of glutamate release from the presynaptic membrane relative to the AMPAR cluster. We found that the annulus-like topography of SGNs enables the EPSC amplitude to be virtually independent of the release location: only 5% decrease in EPSC size for a release at ~250 nm from the center of a 900 nm cluster (Figure 3G; Figure S1C for disk topography). We conclude that a single SV can trigger EPSCs within the experimentally observed amplitude range, supporting the UQR hypothesis.

Finally, we investigated whether glutamate release through successive short (range, 0–500 μs) and small (range, 0–6 nm) SV fusion pore openings could account for multiphasic EPSCs. The fraction of glutamate released increased with both fusion pore width and opening duration (Figure 3H). For example, 50% of the SV glutamate content escaped through a 2 nm wide pore in only ~120 μs. Several such flickers spread in time could elicit a multiphasic EPSC. Alternatively, less than 50% of glutamate escaped in 0.5 ms through a smaller pore (e.g., < 1 nm), which could generate a prolonged EPSC of small amplitude. Using this model, we generated several EPSCs using different pore dynamics and SV glutamate contents (2,000, 3,000, and 4,000 glutamates; Figure 3I). The mean EPSC charge decreased slightly from compact to non-compact EPSCs (by ~7%–20%; Table S2), compatible with our experimental finding of a lower charge of non-compact EPSCs. The EPSC amplitudes ranged from ~100 to ~400 pA, consistent with the EPSCs amplitude range within a single SGN (e.g., Figure 2A). Additionally, due to stochasticity resulting from glutamate diffusion, AMPAR binding and gating, fixed glutamate content generated a distribution of EPSC sizes with a CV of 0.05–0.11 (Table S2). In summary, different fusion pore dynamics and glutamate contents, together with molecular fluctuations in EPSC generation can explain the observed variety of EPSC shapes and sizes. However, we note that parameters such as the glutamate diffusion coefficient, AMPAR density, and synaptic geometry, although not varied here, would also influence the EPSC amplitude.

EPSC Deconvolution Analysis Supports the Hypothesis of Uniquantal Release through a Dynamic Pore for IHC Exocytosis

To further examine whether UQR or MQR governs synaptic transmission at IHCs, we deconvolved experimentally recorded EPSCs into temporal superpositions of underlying "elementary
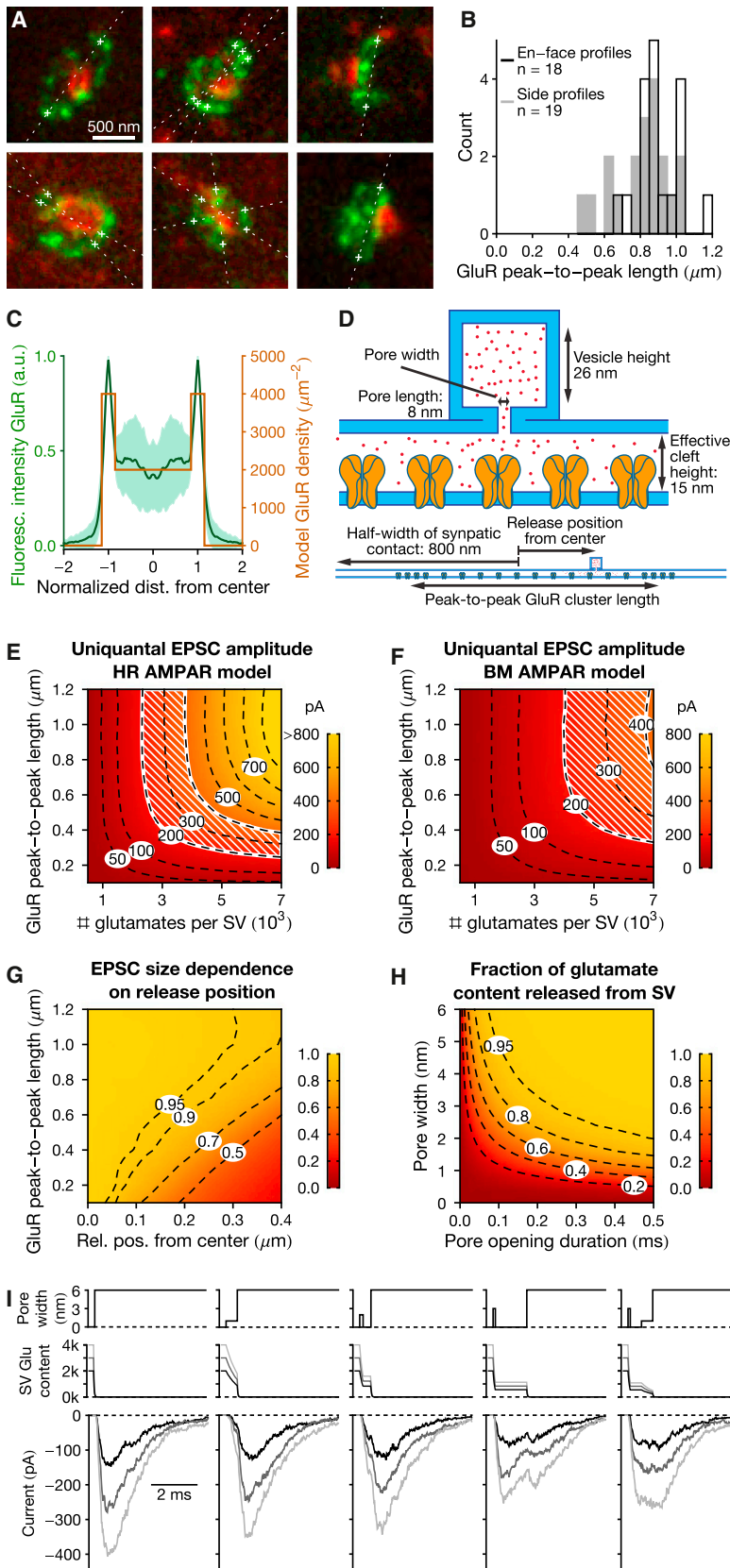
Figure 3. Modeling UQR with a Dynamic Fusion Pore Based on Superresolution Light Microscopy of the AMPAR Clusters

(A–C) 2-color STED images of IHC synapses labeled for the presynaptic AZ (Bassoon, red) and postsynaptic AMPAR cluster (GluR2/3, green). First 2 columns: en-face imaged synapses; last column: side imaged. White dashed lines: line profiles taken to find the peak-to-peak lengths of the AMPAR clusters (B) as well as the average AMPAR cluster profile (C). White crosses: most external peaks positions on the line profiles. (B) Histograms of the AMPAR cluster peak-to-peak lengths in en-face and side profiles. For each synapse where more than one line profile was taken, the average length per synapse was used. En-face: 902 ± 126 nm (n = 18), side: 808 ± 159 nm (n = 19), p = 0.05 (t test). (C) Green (mean ± SD): average GluR density profile. For each synapse, one average line profile was calculated. These lines profiles were then normalized to 1, stretched so that their peaks are aligned at −1 and 1, and averaged. Orange: GluR density profile used in the model.

(D) Scheme of the molecular glutamate release model. The effective synaptic cleft height is smaller than the real height, as it accounts for the true volume available for glutamate diffusion (Savtchenko and Rusakov, 2007). In (E), (F), and (G), glutamate was instantaneously released into the synaptic cleft (i.e., without SV). In (E) and (F), the release position was in the synapse center.

(E) Mean monophasic EPSC amplitude as a function of glutamate amount released into the synaptic cleft and the postsynaptic AMPAR cluster radius. The EPSC amplitude increases with both parameters. The white stripes indicate where the mean EPSC size is between 200 and 400 pA. AMPAR scheme from Häusser and Roth (1997) and AMPAR density profile from (C).

(F) Same as (E) with the AMPAR scheme from Budisantoso et al. (2013).

(G) Normalized monophasic EPSC amplitude as a function of release position for different GluR cluster sizes. For each GluR peak-to-peak length, the EPSC amplitude was set to 1 for a release in the synapse center. AMPAR scheme from Häusser and Roth (1997), AMPAR density profile from (C), and 3,000 glutamates released.

(H) Fraction of glutamate released into the synaptic cleft from a SV for different fusion pore opening durations and widths.

(I) Examples of EPSCs generated with different fusion pore dynamics and SV glutamate contents (2,000, 3,000, and 4,000). Top row: pore width as a function of time; middle row: amount of glutamate remaining in the SV. The first is a monophasic EPSC, the second corresponds to a "foot event"; the third and fourth to multiphasic EPSCs, and the fifth to a prolonged EPSC, not always with apparent multiple peaks. AMPAR scheme from Häusser and Roth (1997), AMPAR density profile from (C), peak-to-peak AMPAR cluster length: 900 nm, release at 200 nm from the synapse center.

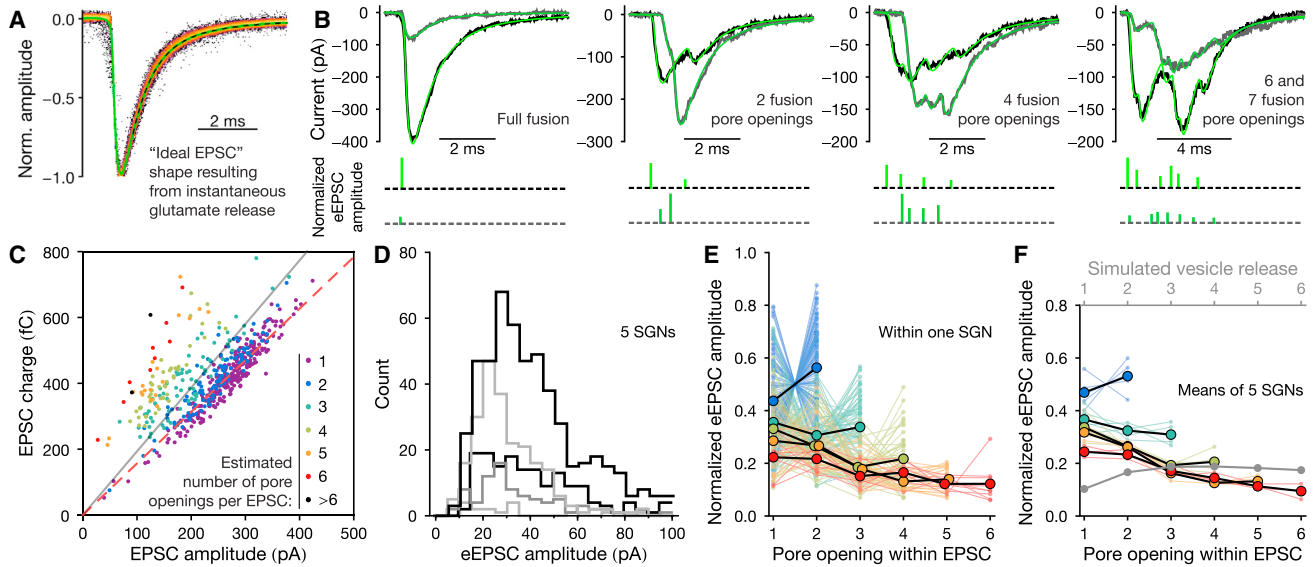See also Figure S1 and Tables S1 and S2.

Figure 4. EPSC Deconvolution into eEPSCs Is Consistent with UQR with a Dynamic Fusion Pore

(A) "Ideal EPSC" (green) constructed by averaging all the normalized EPSCs at the right of the red dashed line from Figure 2E. EPSCs were temporally aligned at the half rise time. The decay of the "ideal EPSC" was well fit by a double exponential (dashed black, time constants $\tau_1 = 0.7$ ms and $\tau_2 = 2.8$ ms with contributions $C_1 = 0.77$ and $C_2 = 0.23$, respectively). Color pseudoscale of the density of all the superimposed EPSCs (n = 203). Same SGN as in Figure 2.

(B) Examples of EPSC deconvolutions. Black/gray: recorded EPSCs; green: reconstructions from the deconvolution signal with 1, 2, 4, and 6–7 underlying eEPSCs, respectively. For each case, two examples are shown. Note the compressed time scale on the far right. The bottom row shows the deconvolution signal: the times and the relative sizes of the underlying eEPSCs. The times approximately correspond to the times of the SV fusion pore opening.

(C) Same scatter plot as in Figure 2E, with colors indicating the number of underlying eEPSCs per EPSC found by deconvolution. Gray line: separation between the blue and red regions in Figure 2E. Red dashed line as in Figure 2E.

(D) Amplitude histogram of the underlying eEPSCs that are separated by at least 0.6 ms from the previous and the next eEPSC within an EPSC. EPSCs made of a single eEPSC are not included. For eEPSCs at the beginning or at the end of an EPSC, only the duration to the next or previous eEPSC needed to be > 0.6 ms, respectively.

(E) Normalized eEPSC sizes for EPSCs composed of two to six eEPSCs. Thin dots and lines represent individual EPSCs, larger dots represent means. Same color code and same SGN as in (C).

(F) Normalized eEPSCs sizes for EPSCs composed of two to six eEPSCs. Thin dots and lines represent means in individual SGNs, larger dots represent their means. The last eEPSC was significantly smaller than eEPSC1 in EPSCs composed of 4 eEPSCs (p = 0.02, n = 5), of 5 eEPSCs (p = 0.001, n = 4), of 6 eEPSCs (p = 0.03, n = 3; paired t test). Gray: normalized eEPSC sizes resulting from an EPSC triggered by the release of 6 × 1,000 glutamates, separated by 0.5 ms, at different positions in the synapse.

See also Figure S2 and Table S1.

EPSCs" (eEPSCs) of different sizes. We defined an eEPSC as an EPSC triggered by glutamate instantaneously liberated into the synaptic cleft. Deconvolution is often employed to estimate quantal release rates, where eEPSCs report the instantaneous release of single SVs (quantal size, $Q = 1$ or miniature [m] EPSC) and their amplitudes are fixed (e.g., Van der Kloot, 1988). Here, for UQR through a dynamic fusion pore, we aimed at revealing the times and nonquantized amounts of glutamate released from a single SV (i.e., in individual EPSCs). Therefore, we only fixed the eEPSC shape to an "ideal EPSC," obtained by normalizing, aligning, and averaging the fastest compact EPSCs for each SGN (Figure 4A), and allowed its size to vary for the deconvolution (e.g., Andor-Ardó et al., 2012). Applying the iterative fitting/deconvolution algorithm on all EPSCs (Figure 4B), we obtained the estimated time and amplitude of all underlying eEPSCs. More temporally spread EPSCs (i.e., with a higher charge over amplitude ratio) were, as expected, composed of more underlying eEPSCs (i.e., pore openings) per EPSC (Figures 4C and S2).

We then examined the amplitude distribution of well-separated eEPSCs (isolated from neighboring eEPSCs by ≥0.6 ms; Figures 4D and S2C). We found that in all SGNs, a wide range of amplitudes down to the detection limit (∼10 pA) was present, consistent with the hypothesis of UQR through a dynamic fusion pore. The absence of a 50 pA peak in the histograms challenges the MQR hypothesis, for which a mean eEPSC (i.e., miniature EPSC) size of ∼50 pA was expected (Glowatzki and Fuchs, 2002; Grant et al., 2010).

For events encompassing several pore openings, the step-by-step emptying of the SV suggests that the successive eEPSC sizes would decrease (Staal et al., 2004). Indeed, in EPSCs made out of four or more eEPSCs, eEPSC1 was significantly larger than the last eEPSC (p < 0.05; Figures 4E and 4F). This decrease could not be explained by AMPAR desensitization: simulating six instantaneous releases of 1,000 glutamates at different positions in the synapse and separated by 0.5 ms, eEPSC1 was the smallest (Figure 4F, gray). For EPSCs composed of two or three eEPSCs, the size of the last eEPSC
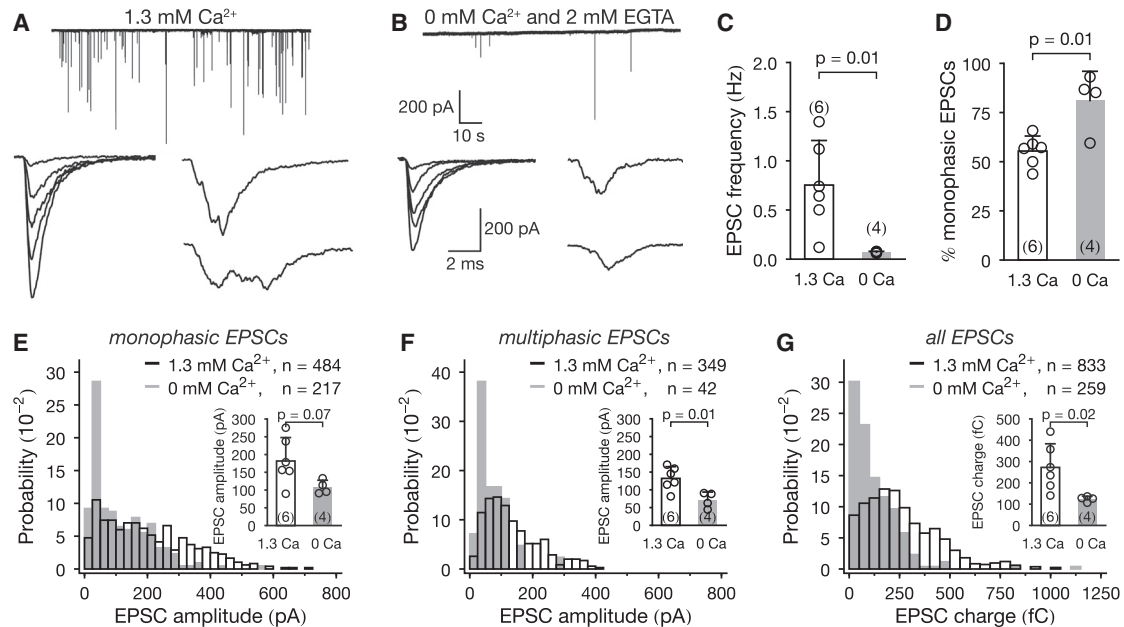
Figure 5. Multiphasic and Large Monophasic EPSCs Persist in the Absence of Ca²⁺ Influx

(A) Sample trace of spontaneous EPSCs recorded from SGNs of a prehearing mice in 1.3 mM $[Ca^{2+}]_e$ (top). Examples of monophasic (bottom left) and multiphasic (bottom right) EPSCs.

(B) Same as (A) in the absence of extracellular Ca^{2+} (0 mM $[Ca^{2+}]_e$ plus 2 mM $[EGTA]_e$). SV release persists in the absence of Ca^{2+} influx.

(C) EPSC frequency in 1.3 mM $[Ca^{2+}]_e$, and 0 mM $[Ca^{2+}]_e$. Numbers in parenthesis denote the number of SGNs.

(D) Percentage of monophasic EPSCs in 1.3 mM $[Ca^{2+}]_e$ and 0 mM $[Ca^{2+}]_e$.

(E) Pooled amplitude distribution for monophasic EPSCs in 1.3 mM $[Ca^{2+}]_e$ (black) and 0 mM $[Ca^{2+}]_e$ (gray). The *n* number indicates the total number of EPSCs in the recordings. Bin width: 20 pA. Inset: mean amplitude of monophasic EPSCs per SGN.

(F) As (E), for multiphasic EPSCs.

(G) As (E), for the charges of all EPSCs. Bin width: 50 fC.

Mann-Whitney U test in (C) and (D); t test in (E)–(G); error bars in (C)–(G) represent the SD. See also Table S3.

was not significantly different from the size of eEPSC1. Even if the amount of glutamate released at the first flicker is the largest, eEPSC1 might still be smaller than eEPSC2 or eEPSC3 due to the nonlinearity of the AMPAR (e.g., Figure 4F, first gray points). In addition, EPSCs with a smaller eEPSC1 relatively to other eEPSCs may reflect pore dilation followed by full fusion ("foot event"). In conclusion, our experimental and modeling findings show that UQR shaped by fusion pore flickering can successfully explain key features of EPSC shape and amplitude heterogeneity at IHC ribbon synapses.

EPSC Heterogeneity Persists when Release Probability Is Reduced by Abolition of IHC Ca²⁺ Influx

An important test of the UQR hypothesis is to study whether EPSC size and shape heterogeneity persists when Ca^{2+} influx is abolished. In fact, if both multiphasic and large monophasic EPSCs arose from MQR via synchronization by a common Ca^{2+} domain build-up around an open Ca^{2+} channel (Graydon et al., 2011; Jarsky et al., 2010)—hereafter termed "Ca^{2+}-synchronized MQR"—these EPSCs should be lost in the absence of Ca^{2+} influx. Therefore, we performed whole-cell patch-clamp recordings from postsynaptic type I SGN boutons of P9–P11 mice in the near absence of extracellular Ca^{2+} ("0 Ca^{2+}": 0 mM added Ca^{2+} and 2 mM EGTA; Figures 5A and 5B). As expected,

the release rate was much lower in "0 Ca^{2+}" than in control (1.3 mM $[Ca^{2+}]_e$; 0.07 Hz versus 0.75 Hz, p = 0.01; Figure 5C).

Despite the massive reduction in exocytosis rate in "0 Ca^{2+}," both multiphasic and large monophasic EPSCs were still present (Figures 5A and 5B). The fraction of monophasic EPSCs was higher in "0 Ca^{2+}" (81% versus 55%, p = 0.01; Figure 5D) and the mean EPSC amplitude and charge were decreased by a factor of ~1.8 (Figures 5E–5G), while EPSC kinetics were not significantly altered (Table S3). These data indicate that Ca^{2+} influx is dispensable for generating EPSC heterogeneity, arguing against the "Ca^{2+}-synchronized MQR" hypothesis of IHC exocytosis. Instead, we favor the interpretation that in the absence of Ca^{2+} influx, SVs exocytose spontaneously and independently of each other. Therefore, both multiphasic and large monophasic EPSCs seem to be triggered by the release of single SVs. We also argue that the increase in the fraction of monophasic EPSCs is compatible with a Ca^{2+} regulation of the fusion pore, as has been reported for the exocytosis of chromaffin granules (Alés et al., 1999; Zhou et al., 1996).

Pharmacological Manipulation of Ca²⁺ Channel Gating Affects the Exocytosis Dynamics

To further investigate the exocytosis mechanism at IHC ribbon synapses, we aimed at modulating the fusion pore dynamics
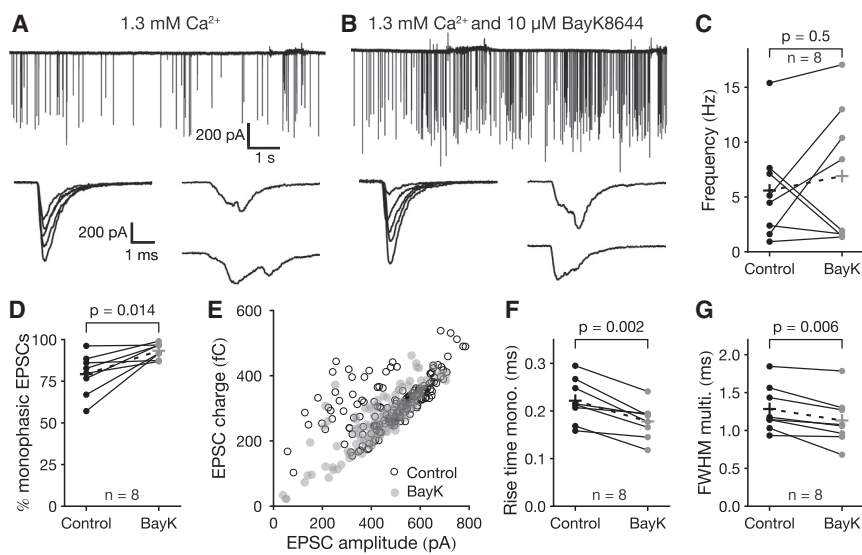
Figure 6. The Ca²⁺ Channel Agonist BayK8644 Promotes Monophasic EPSCs

(A) Sample trace of spontaneous EPSCs recorded from SGNs of a mature rat in 1.3 mM $[Ca^{2+}]_e$ (top). Examples of monophasic (bottom left) and multiphasic (bottom right) EPSCs.

(B) Same SGN as in (A) bath-perfused in 1.3 mM $[Ca^{2+}]_e$ and 10 μM BayK8644.

(C) EPSC frequency in control and BayK8644 conditions. The crosses indicate mean values.

(D) Percentage of monophasic EPSCs in control and BayK8644 conditions.

(E) EPSC charge versus amplitude scatter plot for one SGN. The number of EPSCs in control and BayK8644 conditions was limited to 180 to allow an easier comparison.

(F) Ten percent to ninety percent rise time of monophasic EPSCs in control and BayK8644 conditions.

(G) Full width at half maximum of multiphasic EPSCs in control and BayK8644 conditions.

Wilcoxon signed-rank test in (C) and (D); paired t test (F) and (G). See also Figure S3 and Table S4.

pharmacologically. Because a molecular-scale coupling has been suggested between the SV release machinery and $Ca_V1.3$ Ca²⁺ channels at the mature IHC AZ (Wong et al., 2014) and Ca²⁺ seems to modulate the fusion pore (Figure 5), we examined whether altering Ca²⁺ channel gating may also affect the fusion pore dynamics (Marom et al., 2010). We recorded EPSCs in SGNs of P15–P17 rats under control conditions and then bath-perfused 10 μM BayK8644 (Figures 6A and 6B), a dihydropyridine agonist that promotes long-lasting openings (also called mode 2) of L-type Ca²⁺ channels (Hess et al., 1984). In IHCs, BayK8644 promotes long openings of $Ca_V1.3$ Ca²⁺ channels (Zampini et al., 2013), roughly doubles Ca²⁺ influx and exocytosis (Brandt et al., 2005) and enhances synaptic transmission (Robertson and Paki, 2002). The EPSC rate increased in five of eight SGNs (Figure 6C) without notable change in EPSC amplitude or charge (Figure S3). Independent of changes in EPSC rate, we found a reduced abundance of multiphasic EPSCs in all eight SGNs (Figures 6D and 6E). Additionally, EPSC kinetics got faster: both the rise time of monophasic EPSCs and the full width at half maximum of multiphasic EPSCs decreased in BayK8644 (Figures 6F and 6G). One interpretation is that long $Ca_V1.3$ Ca²⁺ channel openings promoted by BayK8644 may favor full SV fusion, either via a direct molecular coupling between the Ca²⁺ channel and the SV release machinery or because of the longer lasting pulses of Ca²⁺ concentration at the release site.

"Ca²⁺-Synchronized MQR" Hypothesis Seems Incompatible with BayK8644 Findings

Although the "Ca²⁺-synchronized MQR" hypothesis was challenged by the persistence of EPSC heterogeneity in "0 Ca²⁺," we examined its plausibility for the interpretation of the BayK8644 findings using modeling. We aimed to understand whether an increase in Ca²⁺ channel mean open time could enhance release synchrony and thus increase the monophasic EPSCs fraction. For simplicity, we assumed that as a Ca²⁺ chan-

nel opens, the entire pool of $N_{tot} = 14$ readily releasable SVs (Wong et al., 2014) senses a Ca²⁺ concentration $[Ca^{2+}]$ for a given duration T_{pulse} (Figures 7A and 7B). To derive conditions necessary for well-synchronized (i.e., monophasic EPSCs) and poorly synchronized release (i.e., multiphasic EPSCs), we calculated time-dependent SV release probabilities, using a model of Ca²⁺-dependent exocytosis in the IHC (Beutner et al., 2001).

We first studied the effect of $[Ca^{2+}]$ on release synchrony by exploring how well a long ($T_{pulse} = 10$ ms) Ca²⁺ pulse synchronizes the release of multiple SVs (Figures 7C–7F). Increasing $[Ca^{2+}]$ led to a higher peak release rate, to a smaller average release latency and jitter, and thus to a smaller mean release asynchrony T_{async}, which was defined as the time lag between the fusion of two SVs. This measure is a lower bound to the mean time lag between the release of the first and the last SV during a release event. T_{async} first rapidly decreased, but slowly saturated for higher $[Ca^{2+}]$, because of the Ca²⁺-independent rate constant γ of the final release step (here increased to 10 ms⁻¹ from 1.7 ms⁻¹ as in Beutner et al., 2001). We found, that for long Ca²⁺ pulses, the $[Ca^{2+}]$ required to generate monophasic EPSCs is ~250 μM, assuming a $T_{async,\ mono}$ of ~0.22 ms (mean 10%–90% rise time). On the other hand, to generate multiphasic EPSCs, $[Ca^{2+}]$ had to be lower than 80 μM when assuming a $T_{async,\ multi} = 0.8$ ms (mean 10%–90% rise time, a lower bound of their "true" asynchrony).

Next, we studied the effect of Ca²⁺ pulse duration (T_{pulse}) on release synchrony. Shortening T_{pulse} constrained the time window for SV exocytosis essentially to T_{pulse} and as a result could lower T_{async} down to 0.1 ms ($\approx 1/\gamma$, Figures 7G–7I). Although all $[Ca^{2+}]$ could produce low release asynchrony with a short T_{pulse}, only low $[Ca^{2+}]$ was able to trigger multiphasic EPSCs. In addition, shorter T_{pulse} decreased the SV release probability P_{rel} and thus the mean number of SVs exocytosed per release event, N_{rel} (Figure 7J). Monophasic and multiphasic EPSCs are triggered by similar average glutamate content (Figure 2; ~6 SVs, i.e., $N_{rel,\ data} = 6$; Grant et al., 2010). Thus, specific

combinations of $[Ca^{2+}]$ and T_{pulse} are required to generate the N_{rel} and T_{async} of monophasic and multiphasic EPSCs (Figure S4A).

Finally, because Ca^{2+} pulses originate from Ca^{2+} channel openings, T_{pulse} is expected to be exponentially distributed: probability(T_{pulse}) $\propto exp(-T_{pulse}/\tau_{open})$, where τ_{open} is the Ca^{2+} channel mean open time (Figure 7K). We thus calculated T_{async} and N_{rel} as a function of $[Ca^{2+}]$ (10–250 μM) and τ_{open} (0–3 ms; Rodriguez-Contreras and Yamoah, 2001; Zampini et al., 2010, 2013; Figures 7L and 7M). Monophasic EPSCs would be triggered by high $[Ca^{2+}]$ and short Ca^{2+} channel mean open times, whereas multiphasic EPSCs would be triggered by lower $[Ca^{2+}]$ and longer open times. Thus, the "Ca^{2+}-synchronized MQR" hypothesis would predict that longer Ca^{2+} channel mean open times increase the mean asynchrony and EPSC amplitude. However, the BayK8644 data showed a decrease in asynchrony and little change in EPSC amplitude (Figure S3). In summary, the biophysical model argues against the hypothesis that BayK8644 increases the proportion of monophasic EPSCs via "Ca^{2+}-synchronized MQR."

Addressing the Homotypic Fusion Hypothesis of Exocytosis at IHC Synapses

Compound exocytosis following homotypic SV-to-SV fusion has been put forward as another major hypothesis of MQR at ribbon synapses (Edmonds et al., 2004; Matthews and Sterling, 2008). To test its plausibility for the IHC synapse, we first measured the size distributions of ribbon-associated SVs (first row around the ribbon) using electron microscopy (EM) following high-pressure freezing and freeze substitution of organs of Corti after inhibition (0 mM Ca^{2+} added and 5 mM EGTA) and stimulation (5 mM Ca^{2+} and 50 mM $[K^+]_e$) of the IHC synapse (Figures 8A–8F). A compound SV created from the fusion of two 40 nm SVs is expected to be ~57 nm in size. After 15 min stimulation at room temperature, we found a significant increase in the mean SV diameter (47.4 ± 18.7 nm versus 40.3 ± 8.9 nm, p < 0.00001; the fraction of SVs with a diameter >55 nm rose from 3% to 10% (Figure 8E). Separating ribbon-associated SVs in upper (membrane-distal) and lower (membrane-proximal) halves, we found that the larger SVs appearing during stimulation were membrane-distal (Figure 8F). In the lower part of the ribbon, the proportion of >55 nm SVs was smaller than 2% in both conditions and there was only a small increase in the mean SV diameter from inhibited to stimulated conditions (39.4 ± 6.6 nm versus 43.8 ± 10.9 nm, p < 0.00001, Mann-Whitney U test). Large SVs were virtually absent at the lower half of the ribbon.

In the homotypic fusion MQR hypothesis, large EPSCs are triggered by the exocytosis of compound SVs. Per definition, a uniquantal SV has a quantal size $Q = 1$, a SV resulting from the homotypic fusion of n SVs, $Q = n$. Assuming six SVs for a 300 pA EPSC (Grant et al., 2010) and taking into account the EPSC size distribution (Figure S5A), more than 98% of EPSCs are caused by multiquantal release ($Q > 1$) and SVs of the corresponding Q should have been present at the AZ before EPSC generation. If multiquantal SVs have the same exocytosis probability as uniquantal SVs, the proportion of multiquantal SVs at the AZ should be similar to the proportion of multiquantal EPSCs—which was not the case. However, if multiquantal SVs

have a higher release probability, their representation in EM at the AZ might be small.

To test this possibility, we simulated homotypic fusion of SVs undergoing Brownian motion on the synaptic ribbon surface and their subsequent exocytosis (Figures 8G–8J; Table S1; Movies S1 and S2). To model the capture of cytosolic SVs by the ribbon, SVs were replenished at the top of the simulation space, maintaining a minimal SV packing density $\varphi_{min} = 40\%$, which corresponds to a steady-state condition of release (Lenzi et al., 2002). Forces at the top and bottom boundaries constrained SVs to stay inside the simulation space and SV docking was mimicked by strong attachment to the AZ membrane at the bottom of the simulation space (Figure S6A). Two nearby SVs fused stochastically with a rate α_{hom} (Figure 8I) and SVs stochastically exocytosed with a fixed rate $\alpha_{exo} = 3$ Hz per SV (Figure 8J), an effective rate during mild synapse stimulation rate-limiting the SV cycle.

To reproduce the experimental EPSC size distribution we constructed four models of homotypic fusion with increasing complexity. In the first, simplest, model, we assumed that the homotypic fusion rate $\alpha_{hom,1}$ is constant on the whole ribbon. In model 2, we assumed that the homotypic fusion rate $\alpha_{hom,2}$ decayed with the distance z from the AZ with a length constant λ_z (Figure S6D), as may result from a Ca^{2+} concentration gradient (He et al., 2009; Roberts, 1994). Screening a large parameter space with models 1 and 2, we found that they generated exocytic Q distributions that were broad and/or strongly positively skewed (Figures S6B, S6C, S6E, and S6G; Movies S1 and S2), conflicting with experimental ones, which are relatively narrow and symmetric (Figure S5). Release was mostly uniquantal, and increasing homotypic fusion rates led to broadening of the Q distribution tail without altering its mode, because such homotypic fusion is self-amplifying: larger SVs have more neighbors and thus tend to further fuse and grow.

To prevent such unrealistic runaway homotypic fusion, in model 3 the homotypic fusion rate $\alpha_{hom,3}$ decreased both with the distance z from the AZ and with $Q_1 + Q_2$ of 2 interacting SVs (parameterized by λ_Q, Figures 8K and S6F). This model robustly reproduced experimental exocytic Q distributions in terms of distribution mean, CV, and skewness (Figures 8L and S6H). We then compared the SV size distribution predicted by this model on the lower half of the ribbon with the EM data (Figure 8M). The model-predicted histogram of SV diameters had two peaks, one at ~40 nm, corresponding to uniquantal SVs, and one at ~95 nm, corresponding to the peak of the exocytic Q histogram (i.e., five to six SVs). The discrepancy between the predicted and observed Q distributions was 88%, because the expected number of multiquantal SVs in the lower half of the ribbon was much higher than measured.

Finally, in model 4 we aimed to increase the fraction of uniquantal SVs near the AZ. Thus, we allowed SV replenishment everywhere on the ribbon (down to 40 nm from the AZ), and also implemented a strong increase in exocytosis probability with Q: $\alpha_{exo}(Q) \propto 10 \cdot Q \cdot \alpha_{exo}$. This model could still reproduce exocytic Q distribution in a certain parameter region. However, since the mismatch of the predicted SV diameter distribution for the lower half with the EM data was still as high as 67% (Figure 8M), we conclude that MQR via homotypic fusion is
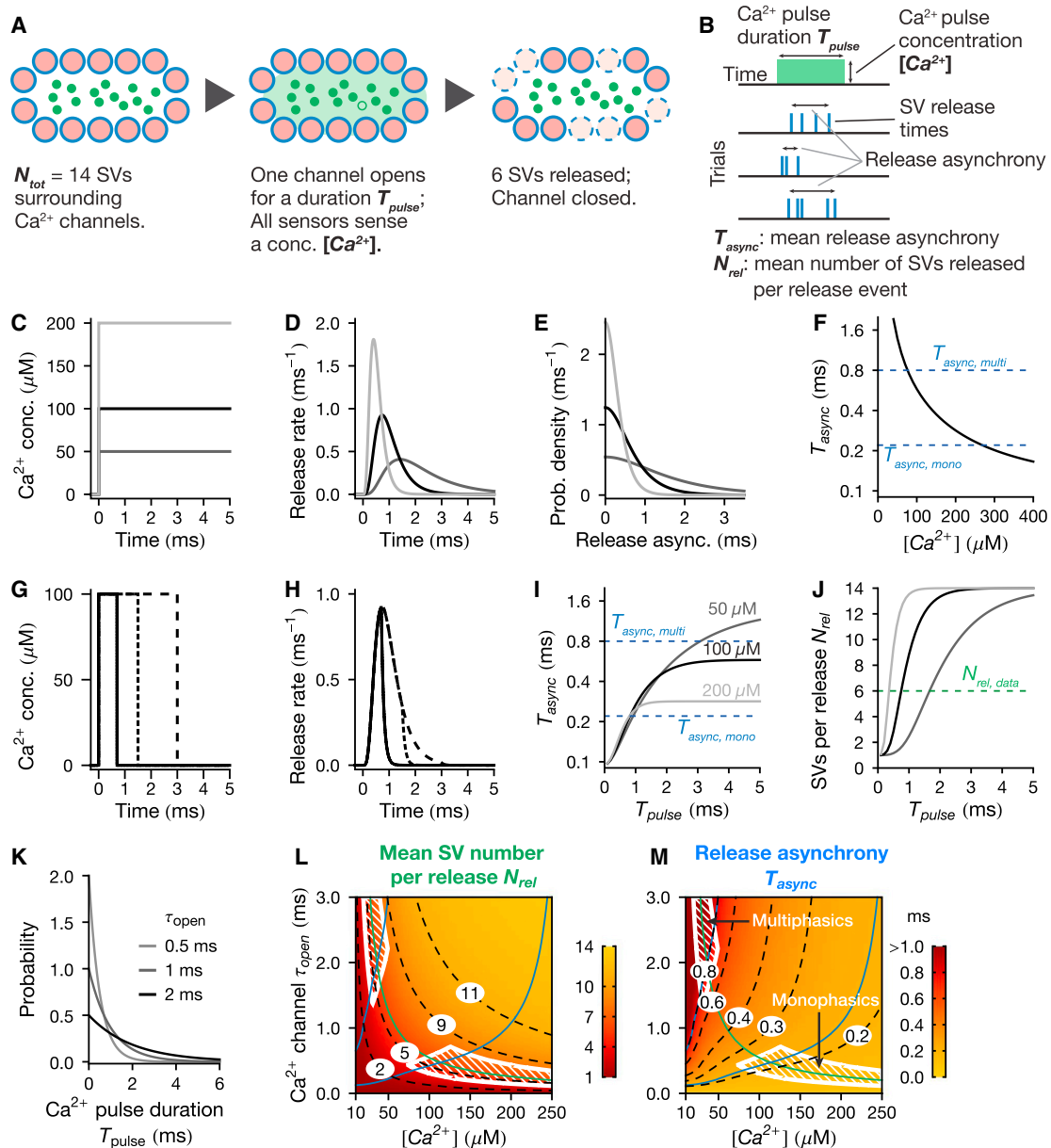
Figure 7. "Ca²⁺-Synchronized MQR" Seems Incompatible with BayK8644 Findings

(A) "Ca²⁺-synchronized MQR" model scheme. Left: N_{tot} = 14 SVs located near several closed Ca²⁺ channels (green disks). Middle: one Ca²⁺ channel opens (green circle) for a duration T_{pulse} and Ca²⁺ sensors located on the SVs sense a Ca²⁺ concentration $[Ca^{2+}]$ (green cloud). Right: 6 SVs were released (dashed circles).

(B) For a Ca²⁺ pulse repeated multiple times, the release asynchrony and the number of SVs released vary.

(C and D) 3 Ca²⁺ pulses of different $[Ca^{2+}]$ and the corresponding release rate time courses calculated with an IHC Ca²⁺-dependent release model (Beutner et al., 2001) with final release rate γ = 10 ms⁻¹.

(E) Probability density distribution of the release asynchrony calculated from the three release rates curves of (D).

(F) Mean release asynchrony T_{async} as a function of $[Ca^{2+}]$. The blue horizontal dashed lines are the mean 10%–90% EPSC rise times of monophasic and multiphasic EPSCs of Figure 6 in control conditions, i.e., $T_{async, mono}$ = 0.22 nm and $T_{async, multi}$ = 0.8 ms, respectively.

(G and H) 3 Ca²⁺ pulses of different duration with $[Ca^{2+}]$ = 100 μM, with corresponding release rate time courses. In (H), the area under the curves gives the SV release probability.

(I) T_{async} as a function of T_{pulse} for three different $[Ca^{2+}]$. Horizontal dashed line as in (F).

(J) Mean number of SVs released per release event (N_{rel}) as a function of T_{pulse}. Release failures (i.e., 0 SVs released) are not part of the mean. The horizontal dashed line represents the experimentally reported mean SV number per EPSC, i.e., $N_{rel, data}$ = 6. Legend as in (I).

(K) In the model, Ca²⁺ pulse durations are exponentially distributed, with different τ_{open}.

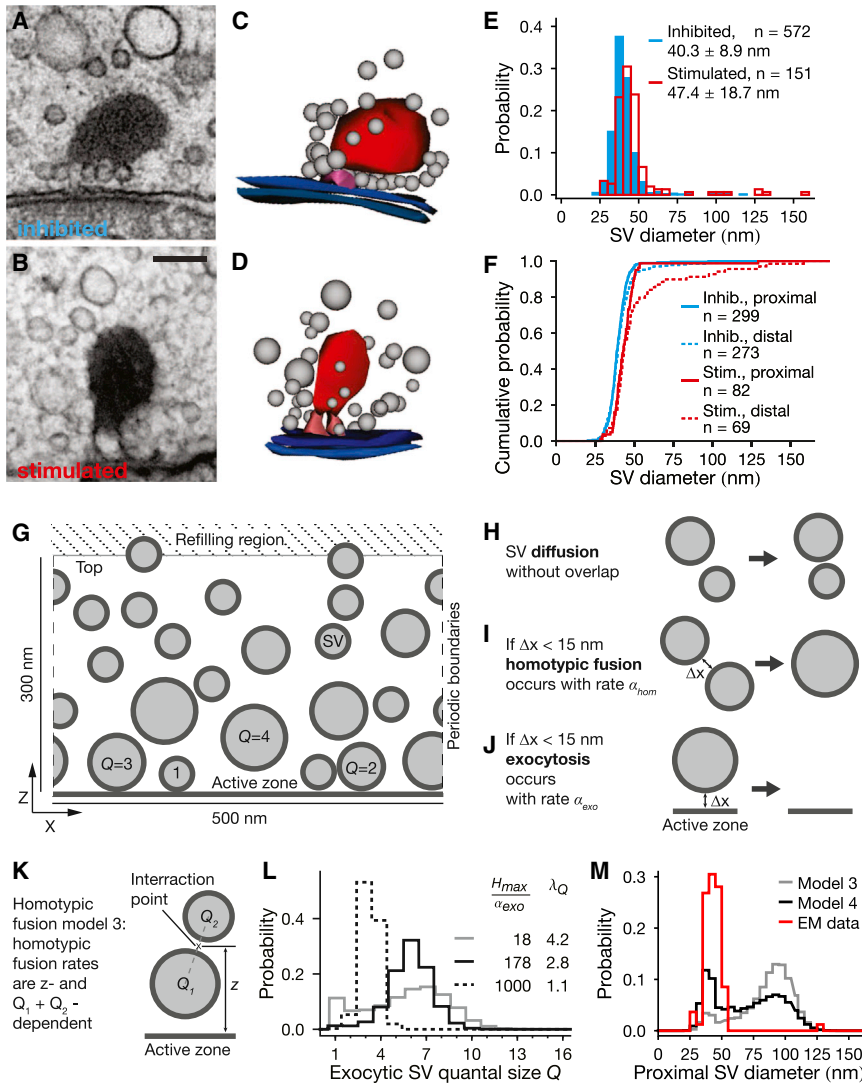*(legend continued on next page)*

Figure 8. Ultrastructural Data Combined with Functional Modeling Reject the Homotypic Fusion Scenario of MQR

(A and B) EM of the IHC ribbon synapse in inhibitory (A) and stimulated (B) conditions. Scale bar, 100 nm.

(C and D) Corresponding 3D reconstructions of serial sections (inhibitory, C; stimulated, D).

(E) Histograms of the SV diameter on the whole ribbon after inhibition (*blue*) or stimulation (*red*). The n numbers represent the total number of SVs. $p < 0.00001$, Mann-Whitney U test.

(F) Cumulative distribution of SV sizes after inhibition (blue) and after stimulation (red) on the lower half (proximal, plain line) and on the upper half (distal, dashed line) of the ribbon. Inhib. prox.: 39.4 ± 6.6 nm, inhib. dist.: 41.3 ± 10.8 nm, stim. prox.: 43.8 ± 10.9 nm, stim. dist.: 51.5 ± 24.5 nm. p values (Mann-Whitney U test): inhib. prox. versus inhib. dist.: 0.2; stim. prox. versus stim. dist.: 0.2; inhib. prox. versus stim. prox.: < 0.00001; inhib. dist. versus stim. dist.: < 0.00001.

(G) Scheme of the homotypic fusion scenario simulation space. The centers of SVs diffuse on a 2D cylinder representing a ribbon of 300 nm height and 500 nm circumference, here depicted as a rectangle with periodic side boundaries. Uniquantal SV diameter: 40 nm.

(H) SVs diffuse without overlap with a diffusion coefficient ($D = 50$ nm^2/ms for uniquantal SVs). D decreases with increasing SV size according to the Einstein-Stokes equation.

(I) Homotypic fusion between two SVs happens with rate α_{hom} when they are closer than 15 nm to each other. The two "parent" SVs vanish and the newly created spherical "daughter" SV emerges in the center of mass of the two "parent" SVs. The glutamate content and total membrane surface are summed.

(J) SVs are exocytosed at rate $\alpha_{exo} = 3$ Hz when closer than 15 nm from the AZ, resulting in the removal of the fused SV from the simulation space.

(K) Homotypic fusion model 3.

(L) Exocytic quantal size histogram from the homotypic fusion model 3 for different values of H_{max}/α_{exo} and λ_Q, with $\lambda_Z = 100$ nm. H_{max} is the maximum homotypic fusion rate, λ_Q indicates how rapidly homotypic fusion rates decrease with $Q_1 + Q_2$.

(M) SV diameter distribution in the lower half of the ribbon from the models 3 and 4 and from EM data. Model parameters for model 3: $H_{max}/\alpha_{exo} = 178$, $\lambda_Q = 2.8$, $\lambda_Z = 100$ nm (see L). The model parameters for model 4 were $H_{max}/\alpha_{exo} = 333$, $\lambda_Q = 3.7$, $\lambda_Z = 100$ nm and could reproduce the exocytic quantal size distribution. The discrepancy between the distributions was calculated as area between the histograms, and divided by 2.

See also Figures S5 and S6, Table S1, and Movies S1 and S2.

---

unlikely to explain EPSC size heterogeneity at IHC ribbon synapses.

DISCUSSION

Dissecting the mechanisms of SV exocytosis is crucial to comprehend synapse functioning and neuronal encoding strategies. We studied the release mechanism at the IHC ribbon synapse, the first synapse in the auditory pathway. Based on biophysical modeling, electrophysiological and ultrastructural experiments, we argue that this synapse operates via UQR through a dynamic fusion pore that is regulated by Ca^{2+} channels and/or Ca^{2+}. We propose that the specific organization of the IHC-SGN synapse enables nearly every single SV release to be

---

(L and M) N_{rel} and T_{async} as a function of the Ca^{2+} concentration during the pulse [Ca^{2+}] and the Ca^{2+} channel mean open time τ_{open}. N_{rel} increases with [Ca^{2+}] and τ_{open}. T_{async} decreases with increasing [Ca^{2+}] and decreasing τ_{open}. The two blue and one green lines correspond to $T_{async, mono}$, $T_{async, multi}$, and $N_{rel, data}$, respectively. The parameter regions to trigger monophasic and multiphasic EPSCs were defined as regions enclosing their mean characteristics: $4 < N_{rel} < 8$; $T_{async} < 0.25$ ms for monophasic EPSCs and $T_{async} > 0.7$ ms for multiphasic EPSCs.

See also Figure S4 and Table S1.

encoded into a spike. This allows the synapse to transmit sound information at spike rates of hundreds of Hertz using an impressive but biologically plausible SV turnover rate.

Uniquantal Release through a Dynamic Fusion Pore Is an Attractive Candidate Mechanism of IHC Exocytosis

We examined UQR through a dynamic fusion pore as a mechanism to explain multiphasic and large monophasic EPSCs at the IHC synapse. In this framework, monophasic (compact) EPSCs result from the instantaneous release of the entire SV glutamate content via one opening of the fusion pore and subsequent full fusion. Fusion pore flickering generates multiphasic (noncompact) EPSCs with different amplitudes and shapes. Evidence supporting the UQR hypothesis at the IHC ribbon synapse includes: (1) measured SV replenishment rates could drive the SGN firing at the recorded spike rates in the UQR scenario, but not in the MQR scenario (Figure 1D). (2) The EPSC charge distribution (mean CV = 0.29) was compatible with a uniquantal EPSC distribution (Figures 2B–2D). (3) Large postsynaptic AMPAR clusters of SGNs could generate large EPSCs in response to release of single SVs (Figures 3E–3G). (4) Different EPSC shapes on average represented a similar glutamate content (Figure 2J) and could be generated with different fusion pore dynamics (Figure 3I). (5) The eEPSC size decrease within EPSCs was compatible with a progressive emptying of a SV, but not with MQR (Figures 4E and 4F). (6) Spontaneous SV release (in "0 Ca^{2+}"), which usually represents independent fusion of single SVs, triggered both multiphasic and large monophasic EPSCs (Figure 5).

Release with varying fusion pore dynamics has recently been reported at retinal bipolar neuron using amperometric detection of artificially loaded norepinephrine (Grabner and Zenisek, 2013). We suggest that the sensitive postsynaptic AMPAR cluster of SGNs together with the recording directly at the postsynaptic bouton allows us to unveil atypical fusion pore opening time courses, which might occur also at other glutamatergic synapses, but might have remained undetected. In fact, the AMPAR cluster embraces the AZ with an annulus-like topography whose size (~900 nm peak-to-peak length, the present study and Meyer et al., 2009) and AMPAR density (3,000 μm^{-2} Saito, 1990) are larger at the IHC synapses than at other synapses (e.g., Masugi-Tokita et al., 2007), thus, allowing an efficient detection of glutamate release. Based on our simulations (Figures 3H and 3I), we propose that pore flickering durations are in the submillisecond range and pore diameter in the low-nanomer range.

At this point, many uncertainties remain regarding the precise number, positioning, conductance, and kinetics of SGN AMPAR receptors, the synaptic geometry, SV glutamate content, glutamate diffusion, and the fusion pore. All these parameters influence the EPSC amplitude. For example, the AMPAR density of 3,000 μm^{-2} (Saito, 1990), which was necessary to reproduce the large EPSCs found in SGNs, might be an overestimation. However, other model values/factors might also differ from reality, still enabling the large EPSCs. For example, the high AMPAR density regions near the SV release sites might increase the glutamate dwelling time due to molecular crowding, thus increasing the EPSC size. Future molecular and biophysical studies will need to further characterize the synapse and test the UQR hypothesis.

Candidate Mechanisms of Multiquantal Release at the IHC Ribbon Synapse

The MQR hypothesis for the IHC ribbon synapse was first introduced by Siegel (1992) and strongly promoted by a landmark paper that provided the first postsynaptic patch-clamp recordings of its EPSCs (Glowatzki and Fuchs, 2002). Since then, MQR has been reported based on postsynaptic recordings at several ribbon synapses (Keen and Hudspeth, 2006; Li et al., 2009; Mehta et al., 2013; Schnee et al., 2013; Singer et al., 2004). Here we tested one proposed scenario at the IHC—synchronized exocytosis driven by a common "Ca^{2+} nanodomain" of a single Ca^{2+} channel—and found it incompatible with our "0 Ca^{2+}" and BayK8644 findings. We also consider the persistence of large EPSCs during strong stimulations that deplete the readily releasable pool (Goutman and Glowatzki, 2007) to further run counter to the hypothesis of "Ca^{2+}-synchronized MQR."

MQR via compound exocytosis was proposed for retinal bipolar neurons and frog saccular hair cells because the membrane equivalent of all ribbon-tethered SVs fused almost immediately (Edmonds et al., 2004; Heidelberger et al., 1994), and based on EM observation of large membranous organelles in the vicinity of the ribbon for retinal bipolar cells (Matthews and Sterling, 2008). Large organelles have also been observed in hair cells (Frank et al., 2010; Lenzi et al., 2002; this study). However, rather than representing exocytic compounds, they have been recently identified as endocytic cisternae reflecting bulk endocytosis (Revelo et al., 2014). Indeed, when analyzing ribbon-proximal SVs in EM, only few large SVs were found and they were mainly positioned on the ribbon upper half, contradicting the prediction of the homotypic fusion model that the majority of AZ-proximal SVs should be multiquantal. Therefore, MQR via compound fusion seemed implausible at the IHC ribbon synapse.

Finally, although our study cannot exclude MQR at the IHC synapse, the maximum known SV replenishment rate (Figure 1D), our deconvolution analysis (Figures 4E and 4F), and the "0 Ca^{2+}" data (Figure 5) argue generally against synchronized MQR at the IHC ribbon synapse, also including scenarios not investigated here such as mechanical synchronization of SVs by the ribbon (Fuchs, 2005; Singer et al., 2004).

Regulation of SV Fusion Pore Dynamics

Our "0 Ca^{2+}" and BayK8644 data suggest that Ca^{2+} and/or the Ca^{2+} channel gating influence the SV fusion pore dynamics. The decrease in EPSC size and charge in our "0 Ca^{2+}" data resemble findings at frog hair cell synapses (Graydon et al., 2011). Within the framework of the UQR hypothesis, one possible explanation is that this decrease reflects Ca^{2+}-dependent regulation of fusion pore dynamics as reported for PC12 and chromaffin cells (Wang et al., 2006; Zhou et al., 1996). Shorter fusion pore flickers in low Ca^{2+} would liberate less glutamate and could explain the lower EPSC size and charge, thus representing subquantal (i.e., incomplete) release. Shorter flickers would also be consistent with the decrease of the multiphasic EPSC fraction and duration in low Ca^{2+}. Alternatively, or in addition, it might reflect a decrease of SV neurotransmitter filling with decreased Ca^{2+} or a decrease in the mean SV diameter, as observed in EM (Figure 8F).

BayK8644, on the other hand, increases the duration of the Ca^{2+} signal elicited by the open Ca^{2+} channel. This could accelerate full SV fusion after fusion pore opening (Wang et al., 2006), compatible with the increase in the monophasic EPSC fraction. Alternatively, the Ca^{2+} channel gating mode could directly influence the fusion pore dynamics (Marom et al., 2010), due to the molecular-scale coupling of Ca^{2+} channels and fusion machinery indicated at the IHC synapse (Brandt et al., 2005; Ramakrishnan et al., 2009; Wong et al., 2014). Such mechanisms could explain the decrease in the multiphasic EPSC fraction occurring with synaptic maturation (Grant et al., 2010) by parallel changes of the Ca^{2+} channel gating (Zampini et al., 2013). Whereas SV fusion pore formation and regulation is not entirely understood (Sørensen, 2009), the pore flickers probably report the operation of fusion proteins (Shi et al., 2012). Their analysis could thus provide important insights into the IHC fusion machinery (Nouvian et al., 2011), when combined with molecular manipulation of candidate proteins such as otoferlin (Pangrsic et al., 2010).

EXPERIMENTAL PROCEDURES

Animal handling and experiments compiled with national animal care guidelines were approved by the University of Göttingen Board for animal welfare and the animal welfare office of the state of Lower Saxony.

Patch-Clamp and STED Microscopy
Whole-cell recordings from postsynaptic boutons of type I SGNs were performed in apical cochlear coils of P9–P11 C57Bl/6 mice and P10–P18 Wistar rats as described previously (Glowatzki and Fuchs, 2002; Rutherford et al., 2012). EPSC were analyzed using Minianalysis (Synaptosoft), Mathematica (Wolfram Resesarch), and Igor Pro (Wavemetrics). Data are expressed as mean ± SD.

STED microscopy of apical cochlear turns from P16 rats immunolabeled for bassoon and GluR2/3 used a custom 2-color-STED microscope (Göttfert et al., 2013).

See the Supplemental Experimental Procedures for further information.

Mathematical Modeling
Monte-Carlo simulations of glutamate release into the synaptic cleft, glutamate diffusion, AMPAR binding and gating were performed in MCell 3.2.1 (http://mcell.org; Kerr et al., 2008) and analyzed in Mathematica (Wolfram Research).

Simulations of SVs release triggered by a rectangular Ca^{2+} pulse of concentration $[Ca^{2+}]$ for a duration T_{pulse}, used the scheme of Ca^{2+}-dependent IHC exocytosis (Beutner et al., 2001). We solved the Master equation for the sensors state occupancy numerically with Mathematica (Wolfram Research).

The dynamics of SVs on the synaptic ribbon surface was implemented as a stochastic simulation, incorporating the Brownian motion of SVs in a fixed 2D geometry, their docking to the AZ, exocytosis, homotypic fusion, and replenishment of the SV pool. Simulations were performed in C++ and analyzed in Mathematica (Wolfram Research). Table S1 summarizes the parameters used for all simulations. See the Supplemental Experimental Procedures for further information.

Electron Microscopy
Apical cochlear coils were explanted and either stimulated or inhibited for 15 min as described previously (Pangrsic et al., 2010). Subsequently, samples were placed in 200 μm/100 μm aluminum planchettes and prepared for high-pressure freezing and freeze-substitution essentially as described previously (Wong et al., 2014). The SV diameter of all SVs in the first row around the ribbon has been determined using the ImageJ software package. Data are expressed as mean ± SD. See the Supplemental Experimental Procedures for further information.

REFERENCES

Albillos, A., Dernick, G., Horstmann, H., Almers, W., Alvarez de Toledo, G., and Lindau, M. (1997). The exocytotic event in chromaffin cells revealed by patch amperometry. Nature *389*, 509–512.

Alés, E., Tabares, L., Poyato, J.M., Valero, V., Lindau, M., and Alvarez de Toledo, G. (1999). High calcium concentrations shift the mode of exocytosis to the kiss-and-run mechanism. Nat. Cell Biol. *1*, 40–44.

Andor-Ardó, D., Hudspeth, A.J., Magnasco, M.O., and Piro, O. (2010). Modeling the resonant release of synaptic transmitter by hair cells as an example of biological oscillators with cooperative steps. Proc. Natl. Acad. Sci. USA *107*, 2019–2024.

Andor-Ardó, D., Keen, E.C., Hudspeth, A.J., and Magnasco, M.O. (2012). Fast, automated implementation of temporally precise blind deconvolution of multiphasic excitatory postsynaptic currents. PLoS ONE *7*, e38198.

Beutner, D., Voets, T., Neher, E., and Moser, T. (2001). Calcium dependence of exocytosis and endocytosis at the cochlear inner hair cell afferent synapse. Neuron *29*, 681–690.

Brandt, A., Khimich, D., and Moser, T. (2005). Few CaV1.3 channels regulate the exocytosis of a synaptic vesicle at the hair cell ribbon synapse. J. Neurosci. *25*, 11577–11585.

Budisantoso, T., Harada, H., Kamasawa, N., Fukazawa, Y., Shigemoto, R., and Matsui, K. (2013). Evaluation of glutamate concentration transient in the synaptic cleft of the rat calyx of Held. J. Physiol. *591*, 219–239.

Chow, R.H., von Rüden, L., and Neher, E. (1992). Delay in vesicle fusion revealed by electrochemical monitoring of single secretory events in adrenal chromaffin cells. Nature *356*, 60–63.

del Castillo, J., and Katz, B. (1954). Quantal components of the end-plate potential. J. Physiol. *124*, 560–573.

Edmonds, B.W., Gregory, F.D., and Schweizer, F.E. (2004). Evidence that fast exocytosis can be predominantly mediated by vesicles not docked at active zones in frog saccular hair cells. J. Physiol. *560*, 439–450.

Frank, T., Rutherford, M.A., Strenzke, N., Neef, A., Pangršič, T., Khimich, D., Fejtova, A., Gundelfinger, E.D., Liberman, M.C., Harke, B., et al. (2010). Bassoon and the synaptic ribbon organize Ca^{2+} channels and vesicles to add release sites and promote refilling. Neuron *68*, 724–738.

Fuchs, P.A. (2005). Time and intensity coding at the hair cell's ribbon synapse. J. Physiol. *566*, 7–12.

Glowatzki, E., and Fuchs, P.A. (2002). Transmitter release at the hair cell ribbon synapse. Nat. Neurosci. *5*, 147–154.

Göttfert, F., Wurm, C.A., Mueller, V., Berning, S., Cordes, V.C., Honigmann, A., and Hell, S.W. (2013). Coaligned dual-channel STED nanoscopy and molecular diffusion analysis at 20 nm resolution. Biophys. J. *105*, L01–L03.

Goutman, J.D., and Glowatzki, E. (2007). Time course and calcium dependence of transmitter release at a single ribbon synapse. Proc. Natl. Acad. Sci. USA *104*, 16341–16346.

Grabner, C.P., and Zenisek, D. (2013). Amperometric resolution of a prespike stammer and evoked phases of fast release from retinal bipolar cells. J. Neurosci. *33*, 8144–8158.

Grant, L., Yi, E., and Glowatzki, E. (2010). Two modes of release shape the postsynaptic response at the inner hair cell ribbon synapse. J. Neurosci. *30*, 4210–4220.

Graydon, C.W., Cho, S., Li, G.-L., Kachar, B., and von Gersdorff, H. (2011). Sharp Ca^{2+} nanodomains beneath the ribbon promote highly synchronous multivesicular release at hair cell synapses. J. Neurosci. *31*, 16637–16650.

Häusser, M., and Roth, A. (1997). Dendritic and somatic glutamate receptor channels in rat cerebellar Purkinje cells. J. Physiol. *501*, 77–95.

He, L., Xue, L., Xu, J., McNeil, B.D., Bai, L., Melicoff, E., Adachi, R., and Wu, L.-G. (2009). Compound vesicle fusion increases quantal size and potentiates synaptic transmission. Nature *459*, 93–97.

Heidelberger, R., Heinemann, C., Neher, E., and Matthews, G. (1994). Calcium dependence of the rate of exocytosis in a synaptic terminal. Nature *371*, 513–515.

Hess, P., Lansman, J.B., and Tsien, R.W. (1984). Different modes of Ca channel gating behaviour favoured by dihydropyridine Ca agonists and antagonists. Nature *311*, 538–544.

Jarsky, T., Tian, M., and Singer, J.H. (2010). Nanodomain control of exocytosis is responsible for the signaling capability of a retinal ribbon synapse. J. Neurosci. *30*, 11885–11895.

Katz, B., and Miledi, R. (1965). The effect of calcium on acetylcholine release from motor nerve terminals. Proc. R. Soc. Lond. B Biol. Sci. *161*, 496–503.

Keen, E.C., and Hudspeth, A.J. (2006). Transfer characteristics of the hair cell's afferent synapse. Proc. Natl. Acad. Sci. USA *103*, 5537–5542.

Kerr, R.A., Bartol, T.M., Kaminsky, B., Dittrich, M., Chang, J.-C.J., Baden, S.B., Sejnowski, T.J., and Stiles, J.R. (2008). Fast Monte Carlo simulation methods for biological reaction-diffusion systems in solution and on surfaces. SIAM J. Sci. Comput. *30*, 3126.

Lenzi, D., Crum, J., Ellisman, M.H., and Roberts, W.M. (2002). Depolarization redistributes synaptic membrane and creates a gradient of vesicles on the synaptic body at a ribbon synapse. Neuron *36*, 649–659.

Li, G.-L., Keen, E., Andor-Ardó, D., Hudspeth, A.J., and von Gersdorff, H. (2009). The unitary event underlying multiquantal EPSCs at a hair cell's ribbon synapse. J. Neurosci. *29*, 7558–7568.

Liu, G. (2003). Presynaptic control of quantal size: kinetic mechanisms and implications for synaptic transmission and plasticity. Curr. Opin. Neurobiol. *13*, 324–331.

Marom, M., Hagalili, Y., Sebag, A., Tzvier, L., and Atlas, D. (2010). Conformational changes induced in voltage-gated calcium channel Cav1.2 by BayK 8644 or FPL64176 modify the kinetics of secretion independently of Ca^{2+} influx. J. Biol. Chem. *285*, 6996–7005.

Masugi-Tokita, M., Tarusawa, E., Watanabe, M., Molnár, E., Fujimoto, K., and Shigemoto, R. (2007). Number and density of AMPA receptors in individual synapses in the rat cerebellum as revealed by SDS-digested freeze-fracture replica labeling. J. Neurosci. *27*, 2135–2144.

Matthews, G., and Sterling, P. (2008). Evidence that vesicles undergo compound fusion on the synaptic ribbon. J. Neurosci. *28*, 5403–5411.

Mehta, B., Snellman, J., Chen, S., Li, W., and Zenisek, D. (2013). Synaptic ribbons influence the size and frequency of miniature-like evoked postsynaptic currents. Neuron *77*, 516–527.

Meyer, A.C., Frank, T., Khimich, D., Hoch, G., Riedel, D., Chapochnikov, N.M., Yarin, Y.M., Harke, B., Hell, S.W., Egner, A., and Moser, T. (2009). Tuning of synapse number, structure and function in the cochlea. Nat. Neurosci. *12*, 444–453.

Neef, A., Khimich, D., Pirih, P., Riedel, D., Wolf, F., and Moser, T. (2007). Probing the mechanism of exocytosis at the hair cell ribbon synapse. J. Neurosci. *27*, 12933–12944.

Nouvian, R., Neef, J., Bulankina, A.V., Reisinger, E., Pangršič, T., Frank, T., Sikorra, S., Brose, N., Binz, T., and Moser, T. (2011). Exocytosis at the hair cell ribbon synapse apparently operates without neuronal SNARE proteins. Nat. Neurosci. *14*, 411–413.

Nusser, Z., Cull-Candy, S., and Farrant, M. (1997). Differences in synaptic GABA(A) receptor number underlie variation in GABA mini amplitude. Neuron *19*, 697–709.

Orrego, F., and Villanueva, S. (1993). The chemical nature of the main central excitatory transmitter: a critical appraisal based upon release studies and synaptic vesicle localization. Neuroscience *56*, 539–555.

Pangrsic, T., Lasarow, L., Reuter, K., Takago, H., Schwander, M., Riedel, D., Frank, T., Tarantino, L.M., Bailey, J.S., Strenzke, N., et al. (2010). Hearing requires otoferlin-dependent efficient replenishment of synaptic vesicles in hair cells. Nat. Neurosci. *13*, 869–876.

Pawlu, C., DiAntonio, A., and Heckmann, M. (2004). Postfusional control of quantal current shape. Neuron *42*, 607–618.

Pickett, J.A., and Edwardson, J.M. (2006). Compound exocytosis: mechanisms and functional significance. Traffic *7*, 109–116.

Rahamimoff, R., and Fernandez, J.M. (1997). Pre- and postfusion regulation of transmitter release. Neuron *18*, 17–27.

Ramakrishnan, N.A., Drescher, M.J., and Drescher, D.G. (2009). Direct interaction of otoferlin with syntaxin 1A, SNAP-25, and the L-type voltage-gated calcium channel Cav1.3. J. Biol. Chem. *284*, 1364–1372.

Revelo, N.H., Kamin, D., Truckenbrodt, S., Wong, A.B., Reuter-Jessen, K., Reisinger, E., Moser, T., and Rizzoli, S.O. (2014). A new probe for super-resolution imaging of membranes elucidates trafficking pathways. J. Cell Biol. *205*, 591–606.

Riveros, N., Fiedler, J., Lagos, N., Muñoz, C., and Orrego, F. (1986). Glutamate in rat brain cortex synaptic vesicles: influence of the vesicle isolation procedure. Brain Res. *386*, 405–408.

Roberts, W.M. (1994). Localization of calcium signals by a mobile calcium buffer in frog saccular hair cells. J. Neurosci. *14*, 3246–3262.

Robertson, D., and Paki, B. (2002). Role of L-type Ca^{2+} channels in transmitter release from mammalian inner hair cells. II. Single-neuron activity. J. Neurophysiol. *87*, 2734–2740.

Rodriguez-Contreras, A., and Yamoah, E.N. (2001). Direct measurement of single-channel Ca^{2+} currents in bullfrog hair cells reveals two distinct channel subtypes. J. Physiol. *534*, 669–689.

Rossi, M.L., Martini, M., Pelucchi, B., and Fesce, R. (1994). Quantal nature of synaptic transmission at the cytoneural junction in the frog labyrinth. J. Physiol. *478*, 17–35.

Rutherford, M.A., Chapochnikov, N.M., and Moser, T. (2012). Spike encoding of neurotransmitter release timing by spiral ganglion neurons of the cochlea. J. Neurosci. 32, 4773–4789.

Saito, K. (1990). Freeze-fracture organization of hair cell synapses in the sensory epithelium of guinea pig organ of Corti. J. Electron Microsc. Tech. 15, 173–186.

Savtchenko, L.P., and Rusakov, D.A. (2007). The optimal height of the synaptic cleft. Proc. Natl. Acad. Sci. USA 104, 1823–1828.

Savtchenko, L.P., Sylantyev, S., and Rusakov, D.A. (2013). Central synapses release a resource-efficient amount of glutamate. Nat. Neurosci. 16, 10–12.

Schnee, M.E., Castellano-Muñoz, M., and Ricci, A.J. (2013). Response properties from turtle auditory hair cell afferent fibers suggest spike generation is driven by synchronized release both between and within synapses. J. Neurophysiol. 110, 204–220.

Shi, L., Shen, Q.T., Kiel, A., Wang, J., Wang, H.W., Melia, T.J., Rothman, J.E., and Pincet, F. (2012). SNARE proteins: one to fuse and three to keep the nascent fusion pore open. Science 335, 1355–1359.

Siegel, J.H. (1992). Spontaneous synaptic potentials from afferent terminals in the guinea pig cochlea. Hear. Res. 59, 85–92.

Singer, J.H., Lassová, L., Vardi, N., and Diamond, J.S. (2004). Coordinated multivesicular release at a mammalian ribbon synapse. Nat. Neurosci. 7, 826–833.

Sørensen, J.B. (2009). Conflicting views on the membrane fusion machinery and the fusion pore. Annu. Rev. Cell Dev. Biol. 25, 513–537.

Staal, R.G.W., Mosharov, E.V., and Sulzer, D. (2004). Dopamine neurons release transmitter via a flickering fusion pore. Nat. Neurosci. 7, 341–346.

Suryanarayanan, A., and Slaughter, M.M. (2006). Synaptic transmission mediated by internal calcium stores in rod photoreceptors. J. Neurosci. 26, 1759–1766.

Taberner, A.M., and Liberman, M.C. (2005). Response properties of single auditory nerve fibers in the mouse. J. Neurophysiol. 93, 557–569.

Takamori, S., Holt, M., Stenius, K., Lemke, E.A., Grønborg, M., Riedel, D., Urlaub, H., Schenck, S., Brügger, B., Ringler, P., et al. (2006). Molecular anatomy of a trafficking organelle. Cell 127, 831–846.

Van der Kloot, W. (1988). Estimating the timing of quantal releases during end-plate currents at the frog neuromuscular junction. J. Physiol. 402, 595–603.

Wadiche, J.I., and Jahr, C.E. (2001). Multivesicular release at climbing fiber-Purkinje cell synapses. Neuron 32, 301–313.

Wang, C.-T., Bai, J., Chang, P.Y., Chapman, E.R., and Jackson, M.B. (2006). Synaptotagmin-Ca^{2+} triggers two sequential steps in regulated exocytosis in rat PC12 cells: fusion pore opening and fusion pore dilation. J. Physiol. 570, 295–307.

Wong, A.B., Rutherford, M.A., Gabrielaitis, M., Pangrsic, T., Göttfert, F., Frank, T., Michanski, S., Hell, S., Wolf, F., Wichmann, C., and Moser, T. (2014). Developmental refinement of hair cell synapses tightens the coupling of Ca^{2+} influx to exocytosis. EMBO J. 33, 247–264.

Zampini, V., Johnson, S.L., Franz, C., Lawrence, N.D., Münkner, S., Engel, J., Knipper, M., Magistretti, J., Masetto, S., and Marcotti, W. (2010). Elementary properties of CaV1.3 Ca^{2+} channels expressed in mouse cochlear inner hair cells. J. Physiol. 588, 187–199.

Zampini, V., Johnson, S.L., Franz, C., Knipper, M., Holley, M.C., Magistretti, J., Masetto, S., and Marcotti, W. (2013). Burst activity and ultrafast activation kinetics of CaV1.3 Ca^{2+} channels support presynaptic activity in adult gerbil hair cell ribbon synapses. J. Physiol. 591, 3811–3820.

Zhou, Z., Misler, S., and Chow, R.H. (1996). Rapid fluctuations in transmitter release from single vesicles in bovine adrenal chromaffin cells. Biophys. J. 70, 1543–1552.